Surface Contribution to Planetary Albedo Variability in Cryosphere Regions

XIN QU AND ALEX HALL

Department of Atmospheric and Oceanic Sciences, University of California, Los Angeles, Los Angeles, California

ABSTRACT

Climatological planetary albedo obtained from the International Satellite Cloud Climatology Project (ISCCP) D-series flux dataset is broken down into contributions from the surface and atmosphere in cryosphere regions. The atmosphere accounts for much more of climatological planetary albedo ($\geq 75\%$) than the surface at all times of the year. The insignificance of the surface contribution over highly reflective cryosphere regions is attributed mostly to the damping effect of the atmosphere. The overlying atmosphere attenuates the surface's contribution to climatological planetary albedo by reducing the number of solar photons initially reaching the surface and the number of photons initially reflected by the surface that actually reach the top of the atmosphere.

The ISCCP datasets were also used to determine the relative contributions of the surface and atmosphere to seasonal and interannual planetary albedo variability in cryosphere regions. Even damped by the atmosphere to the same degree as in the climatological case, the surface contribution dominates the variability in planetary albedo on seasonal and interannual time scales. The surface accounts for about 75% of the change in climatological planetary albedo from one season to another with similar zenith angle and more than 50% of its interannual variability at nearly all times of the year, especially during seasons with extensive snow and sea ice extent. The dominance of the surface in planetary albedo variability is because surface albedo variability associated with snow and ice fluctuations is significantly larger than atmospheric albedo variability due to cloud fluctuations. The large effect of snow and ice variations on planetary albedo variability suggests that if cloud fields do not change much in a future warmer climate, a retreat of snow cover or sea ice would lead to a significant increase in net incoming solar radiation, resulting in an enhancement of high-latitude climate sensitivity.

1. Introduction

Using an energy balance climate model, Budyko (1969) and Sellers (1969) hypothesized that if incoming solar energy and the transparency of the atmosphere to terrestrial radiation are prescribed, the earth's surface temperature is largely controlled by planetary albedo. The connection of planetary albedo to the thermal state of the surface motivated the climate community to measure this quantity. Numerous estimates have led to a consensus that on a global-mean, annual-mean basis, about 30% of incoming solar photons at the top of the atmosphere (TOA) are reflected back to space by the current climate system (Kiehl and Trenberth 1997).

On a global-mean, annual-mean basis, a larger por-tion of these upwelling solar photons is reflected by the atmosphere rather than the surface (Liou 1992; Grotjahn 1993; Kiehl and Trenberth 1997). This is also largely true even in cryosphere regions, where the surface is highly reflective of solar radiation (e.g., see Fig. 4 of this study). This dominance of the atmosphere probably stems from two effects: first, incoming solar photons at the TOA are partially absorbed and reflected back to space by the atmosphere, reducing the number of photons reaching the surface; second, solar photons initially reflected by the surface are partially absorbed and reflected back to the surface by the atmosphere, and thus only a small portion of them actually reach the TOA. These both can be thought of as a damping effect of the atmosphere on the surface contribution.

Planetary albedo in each location varies on seasonal and interannual time scales. In snow-free land and ice-free ocean, surface albedo variations are small, and most planetary albedo variability stems from variations

Corresponding author address: Xin Qu, Department of Atmospheric and Oceanic Sciences, University of California, Los Angeles, Los Angeles, CA 90095.
E-mail: xinqu@atmos.ucla.edu

in the atmosphere, most likely from clouds. In contrast, surface albedo in cryosphere regions changes significantly on these time scales because of fluctuations in sea ice and snow. These surface albedo variations may be damped by the atmosphere just as the surface contribution to climatological planetary albedo is attenuated by the atmosphere. It is unclear to what extent this damping effect prevents surface albedo fluctuations from being seen in planetary albedo variability. Moreover, fluctuations in atmospheric constituents, such as clouds, result in variability in the albedo of the atmosphere. The effect of these fluctuations on planetary albedo may or may not overwhelm the planetary albedo anomalies resulting from surface albedo fluctuations. The main goal of this study is to quantify the relative contributions of the surface and atmosphere to seasonal and interannual planetary albedo variability over cryosphere regions. This is accomplished by breaking down seasonal and interannual anomalies in planetary albedo obtained from the International Satellite Cloud Climatological Project (ISCCP) D-series cloud and flux datasets into surface and atmospheric contributions.

The extent to which surface albedo fluctuations contribute to observed planetary albedo variability is related to the effectiveness of surface albedo feedback in the real climate. In both energy balance models and GCMs (Budyko 1969; Sellers 1969; Robock 1983; Manabe and Stouffer 1980; Hall 2004; etc.), snow and ice retreat and are replaced by land and ocean surfaces that are much less reflective of solar radiation when the climate becomes warmer. The additional absorbed solar radiation results in more warming, especially in the regions of the snow and ice reduction. This surface albedo feedback amplifies the initial perturbation of the simulated climate and acts as a positive feedback. It is unclear how powerful surface albedo feedback is in the real climate. Its effectiveness is determined partly by the extent to which the overlying atmosphere attenuates surface albedo fluctuations. If the atmosphere were so opaque as to prevent any surface albedo fluctuations from modifying planetary albedo, there would be no surface albedo feedback. On the other hand, if the atmosphere were relatively transparent to solar radiation, then surface albedo fluctuations would translate directly into anomalies in planetary albedo, and surface albedo feedback could be quite powerful. By examining surface and cloud contributions to planetary albedo variability through the ISCCP D-series cloud and flux datasets, we assess which of these alternatives best describes the real climate.

Moreover, because planetary albedo anomalies induced by the surface can be amplified or diminished by planetary albedo anomalies induced by cloud anomalies that coincide with snow and ice anomalies, the effectiveness of surface albedo feedback can be modified by cloud–cryosphere covariability. If cloud anomalies are in phase with snow and ice albedo anomalies, then surface albedo feedback is amplified. On the other hand, if cloud anomalies are out of phase with snow and ice albedo anomalies, then surface albedo feedback is diminished. By examining cloud–cryosphere covariability through the ISCCP cloud and flux datasets, we evaluate which of these alternatives is seen in the real climate.

This study is presented as follows: The ISCCP D-series cloud and flux datasets are described in section 2, followed by a background discussion of distributions of surface and planetary albedos in section 3. An analytical expression for planetary albedo is derived in section 4. The contributions of the surface and atmosphere to seasonal and interannual planetary albedo variability are discussed in section 5. Summary and implications are found in section 6. The sensitivity of our result to the potential bias in the ISCCP datasets is examined in the appendix.

2. Datasets

The ISCCP D-series cloud datasets used in this study are based on observations from a suite of operational weather satellites measuring the temporal and spatial distribution of visible (VIS; wavelength ≈ 0.6 μm), near-infrared (NIR; wavelength ≈ 3.7 μm), and infrared (IR; wavelength ≈ 11 μm) radiation. These measurements are then employed to retrieve information about clouds, such as cloud cover, cloud optical thickness, and cloud-top pressure (Rossow and Schiffer 1991; Rossow and Garder 1993a,b; Rossow et al. 1993; Rossow and Schiffer 1999). Three changes have been made in the D-series datasets to enhance the accuracy of cloud detection over snow- and ice-covered surfaces (Rossow and Schiffer 1999): 1) most importantly, a new threshold test on 3.7-μm radiances was used, exploiting significantly greater contrast between cloudy and clear scenes over snow- and ice-covered surfaces at this frequency than at 0.6 μm; 2) at the high latitudes, the visible radiance threshold test was changed to a visible reflectance threshold test; and 3) over snow and ice in the polar regions, both the VIS and IR thresholds were lowered. Together these improvements have been shown to increase significantly low-level cloud detection sensitivity over snow and ice and reduce the biases in cloud optical thickness of previous ISCCP C-series datasets in these regions.

Accompanying the ISCCP D-series cloud datasets

are radiative flux datasets containing solar and infrared radiative fluxes at the TOA and surface for both clear-sky and full-sky situations. They are calculated by specifying the following information in a radiative transfer model (Zhang et al. 2004): 1) atmospheric temperature and humidity profiles; 2) vertical profiles of various atmospheric gases, such as CO_2, O_3, O_2, and CH_4; 3) vertical aerosol profiles for the troposphere and stratosphere; 4) ISCCP D-series cloud datasets; and 5) snow and ice cover data. All the data mentioned above are time varying so that observed variations in radiative properties of the atmosphere and surface are reflected in the fluxes at the TOA and surface.

3. Distribution of surface and planetary albedos

In this section, we characterize the seasonal and geographical distribution of surface and planetary albedos, calculated from the ISCCP shortwave fluxes, as well as their interannual variability during the 17-yr period of ISCCP (1984–2000).

a. Seasonal cycle

Figure 1a shows the seasonal and geographical distribution of surface albedo. This quantity exhibits large spatial variations during all seasons. It is highest in snow- and ice-covered areas and lowest in ice-free oceans and snow-free land areas. In the Sahara and Saudi Arabia deserts, intermediate values of surface albedo are found. Surface albedo in Northern Hemisphere (NH) extratropical land areas displays large seasonal variations. During December–January–February (DJF; hereafter, 3-month periods are denoted by the first letter of each respective month), high surface albedo dominates nearly all the NH extratropical land areas, consistent with large wintertime snow extent in Eurasia and North America (Robinson et al. 1993). In MAM, highly reflective regions move northward in accordance with the springtime retreat of snowpack. Because of the near disappearance of snow from the NH continents in summertime, the land surface becomes somewhat darker. During SON, surface albedo is as low as in JJA in nearly all the NH land areas with the exception of Alaska and northern Siberia, where slightly higher surface albedo occurs because of the autumnal growth of snow cover.

Surface albedo also shows large seasonal variations in the Arctic and the circumpolar ocean. In the Arctic, the surface is brighter in MAM than JJA and SON. This is consistent with the fact that Arctic sea ice extent is larger in spring than summer and fall (Vinnikov et al. 2002). However, the surface in the Arctic is much

darker in DJF than MAM, in spite of fact that Arctic sea ice extent is about as large in DJF as MAM. This is attributable to a bias in ISCCP in the calculation of surface albedo in polar regions when insolation is extremely small during winter (Y.-C. Zhang 2004, personal communication). Because this bias makes polar surface albedo less trustworthy during winter, and because wintertime surface albedo over the poles is not very meaningful in any case, we disregard the Arctic and circumpolar ocean during winter throughout the remainder of this paper. Surface albedo in the Arctic is slightly smaller in SON than JJA, consistent with the fact that sea ice extent reaches a minimum in September (Vinnikov et al. 2002). Surface albedo in the circumpolar ocean is highest in SON, lowest in MAM, and in between during DJF, consistent with the seasonal variations of sea ice extent in this region (Vinnikov et al. 2002).

Figure 1b shows the seasonal and geographical distribution of planetary albedo. The spatial variations in this quantity are somewhat similar to those in surface albedo, but with smaller amplitude. The signatures of the seasonal variations of surface albedo in NH land areas, the Arctic, and the circumpolar ocean are visible in the patterns in planetary albedo. This suggests that the surface may play an important role in generating the seasonal variations of planetary albedo in snow- and ice-covered areas.

b. Interannual variability

Figure 2a shows the seasonal and geographical distribution of surface albedo variability. This quantity exhibits large variations during all seasons due to snow variability on NH land masses, though the patterns differ from one season to another. During DJF, two maxima stretch from western Europe to central Asia and along the border between Canada and the United States. These coincide with excursions of the wintertime snow margin in Eurasia and North America (Walland and Simmonds 1997). Large variations also occur in central Russia and Alaska boreal forest zones. These anomalies in the snowpack interior may result from variations in snow depth (Robock 1980; Kukla and Robinson 1980). In addition, surface albedo within snow-covered forests can be affected by the quantity of snow remaining on the forest canopy (Laine and Heikinheimo 1996). Finally, local surface temperature can generate surface albedo anomalies in the snowpack by modifying the properties of the snow (e.g., wet melting snow has lower surface albedo than dry frozen snow). During MAM the two continental wintertime maxima migrate poleward with reduced amplitudes.

(a) climatological surface albedo

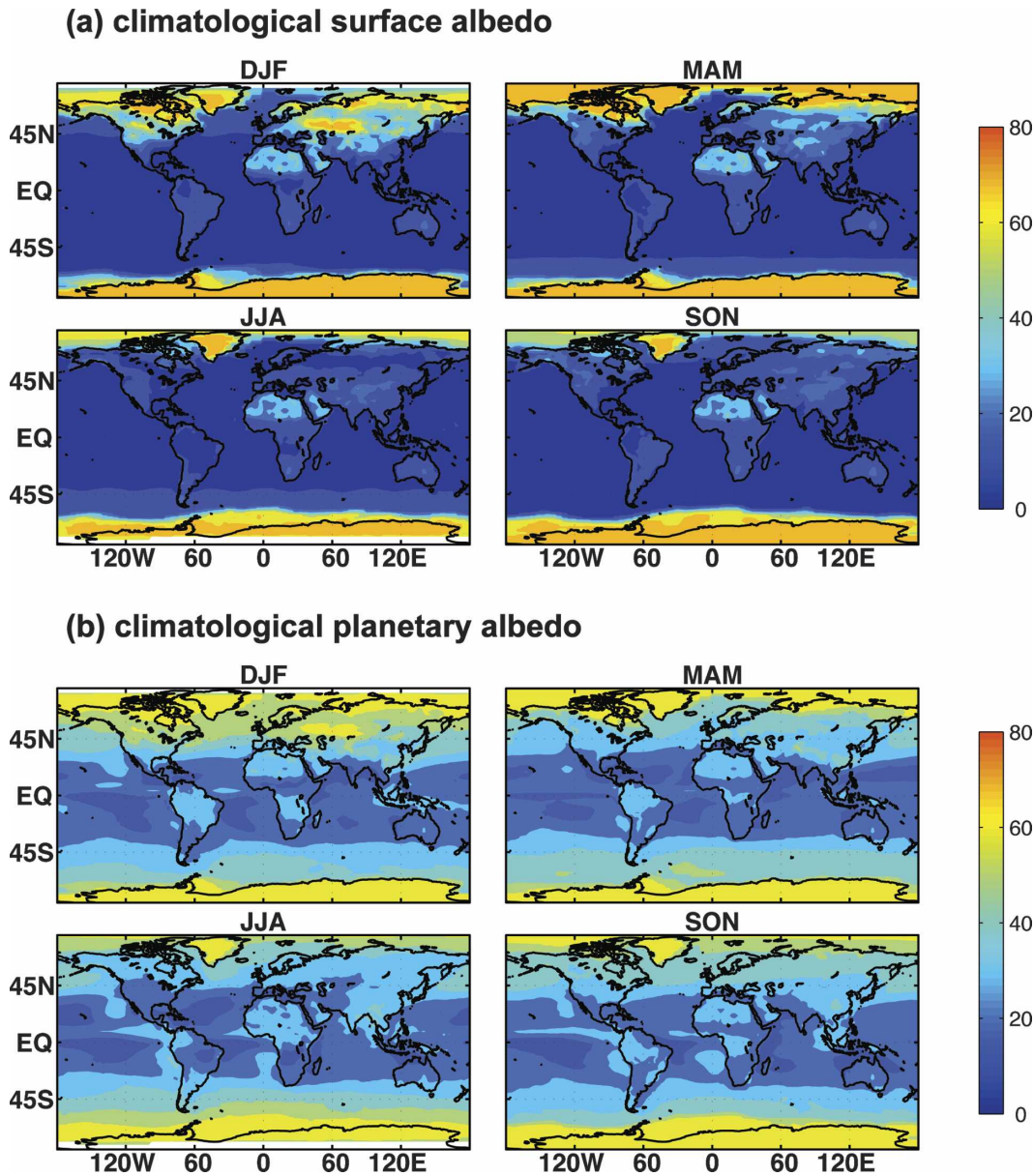
(b) climatological planetary albedo

FIG. 1. The geographical distribution of climatological seasonal-mean (a) surface and (b) planetary albedo (%). Climatological seasonal-mean shortwave radiative fluxes at the (a) surface and (b) TOA were first calculated based on the ISCCP D-series flux dataset. (a) Surface and (b) planetary albedo was then calculated by taking the ratio of upwelling to downwelling fluxes at the (a) surface and (b) TOA. Note that the ISCCP cloud and flux datasets used in this work are provided on a global 2.5° × 2.5° grid and cover the period from 1984 to 2000 at 3-h temporal resolution.

This corresponds to the springtime retreat of the snow margin. In JJA only a small portion of northern Russia near the Arctic shows significant variations in surface albedo, consistent with the near disappearance of snow from the NH continents. During SON, large surface albedo variations are found in high latitudes due to the autumnal growth of snow cover, particularly over Alaska and northern Siberia.

In the NH sea ice zone, significant variations in surface albedo are confined to the Labrador, Greenland, Barents, and Bering Seas during MAM but are displaced northward to areas of the Arctic adjacent to the Eurasian and North American continents during JJA and SON. This seasonal dependence corresponds with the seasonal migration of the NH sea ice margin (Parkinson 1991). Nearly the entire Arctic basin is covered
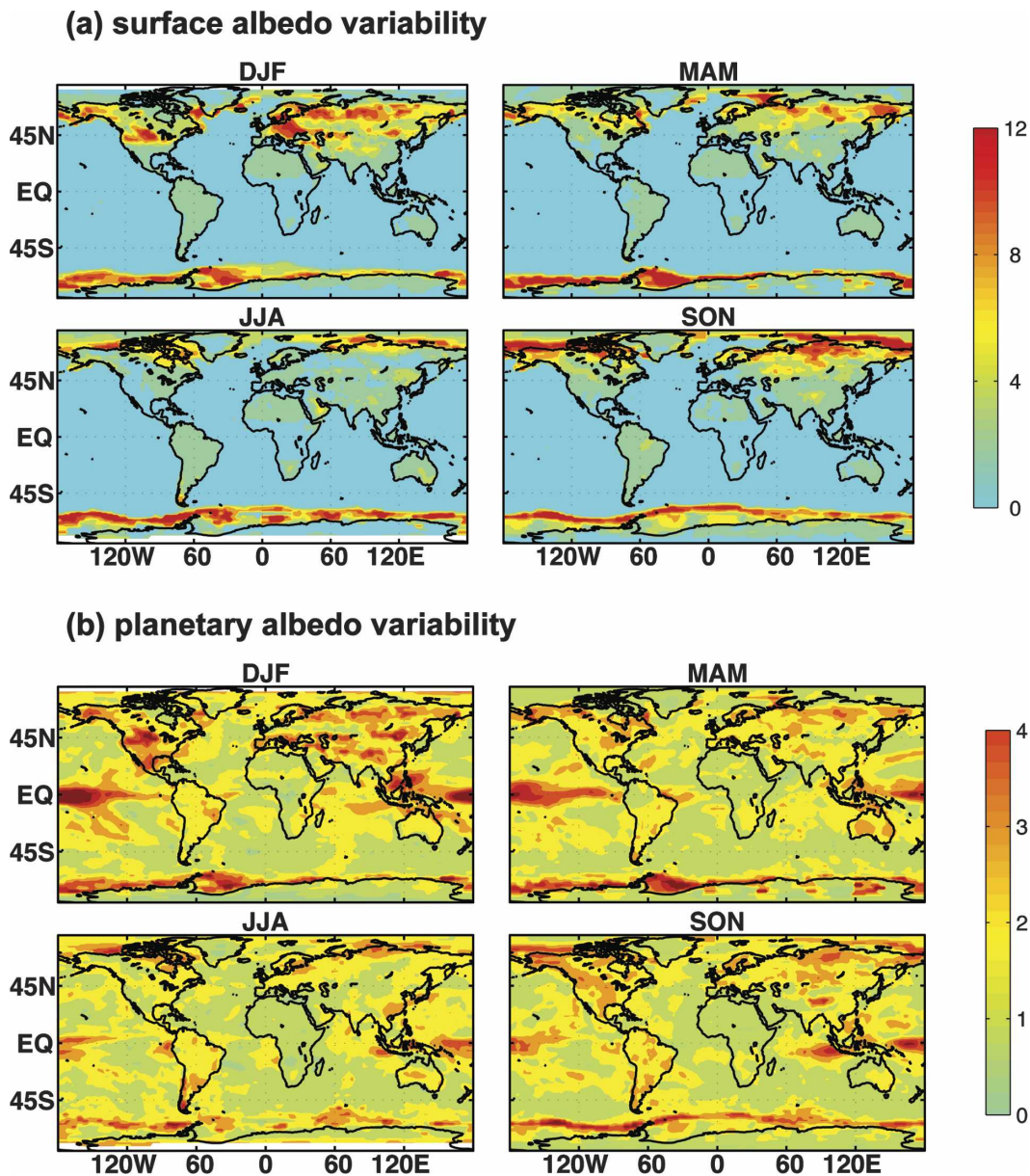
FIG. 2. The geographical distributions of std dev of (a) surface and (b) planetary albedo (%). Seasonal-mean shortwave radiative fluxes at the (a) surface and (b) TOA were first calculated based on the ISCCP D-series flux dataset. Then, (a) surface and (b) planetary albedo was calculated by taking the ratio of upwelling to downwelling fluxes at the (a) surface and (b) TOA. Finally, std devs of surface and planetary albedo were calculated based on (a) surface and (b) planetary albedo time series at each location. Note that the color bar in (a) is different from that of (b).

by sea ice in MAM, and thus variations in the ice margin are displaced to areas adjacent to the northern North Atlantic and North Pacific Oceans. During NH summertime, sea ice retreats northward, confined for the most part to the Arctic. Larger variations develop in broader regions during SON than during JJA, in spite of the fact that the ice margin is located at approximately the same location during both seasons. This is consistent with the seasonality of Arctic sea ice

variability. Parkinson (1991) observed that during NH fall, more sea ice variability occurs over a broader area of the Arctic than during other seasons.

In the circumpolar ocean during all seasons, variations in surface albedo are distributed more or less uniformly over all longitudes. However, their magnitude and approximate latitude vary seasonally. During DJF, variations are confined to the ocean adjacent to the Antarctic coast. Slightly larger surface albedo varia-

tions are found in these same areas in MAM and then are displaced northward during SON. As in the NH sea ice zone, these features are consistent with the seasonal variation of the sea ice margin in the circumpolar ocean (Parkinson 1992; Gloersen et al. 1999). In SH summertime (DJF), sea ice melts and retreats to the oceans adjacent to the Antarctic coast. During MAM and JJA, sea ice grows rapidly, pushing the ice margin northward. In SON, sea ice grows during the first part of the season and melts during the second part, so the seasonal-mean ice margin is found at approximately the same location as in JJA.

The signatures of surface albedo variability due to the fluctuations in the cryosphere are visible in the patterns in planetary albedo variability, shown in Fig. 2b. The maxima in surface albedo variability over 1) NH snow-covered lands during DJF, MAM, and SON; 2) NH sea ice zone during JJA and SON; and 3) SH sea ice zone during all seasons all correspond to local maxima in planetary albedo variability in Fig. 2b. This suggests that variations in surface albedo make a significant contribution to interannual variability of planetary albedo at these locations. However, the amplitudes of these maxima in planetary albedo variability are about 3 times smaller than their surface albedo counterparts. The patterns of planetary albedo variability in regions where the cryosphere dominates surface albedo variability also do not match the patterns of surface albedo variability perfectly, suggesting atmospheric variations, most likely clouds, play some role in generating interannual variability of planetary albedo in these regions.

4. An analytical expression for planetary albedo

In this section, we use an idealized radiative transfer model to obtain an analytical expression for planetary albedo. In this model, incoming solar radiation at the TOA (I_t) first travels through the atmosphere. Part of it ($R_t^{(1)}$) is reflected directly back to space, and part of it ($I_s^{(1)}$) reaches the surface, where multiple reflection between the surface and atmosphere is initiated (see Fig. 3). Total upwelling solar radiative flux at the TOA (R_t) can be expressed as a function of incoming solar radiative flux at the TOA and shortwave radiative properties of the surface and atmosphere as follows (see notation in Table 1):

$$R_t = R_t^{(1)} + R_t^{(2)} + R_t^{(3)} + \cdots$$
$$= I_t\alpha_\downarrow + I_t T_\downarrow \alpha_s^{(1)} T_\uparrow^{(1)} + I_t T_\downarrow \alpha_s^{(1)} \alpha_\uparrow^{(1)} \alpha_s^{(2)} T_\uparrow^{(2)} + \cdots.$$

$$(1)$$

To obtain an analytical expression for planetary albedo, we assume $\alpha_s^{(n)} = \alpha_s^{(1)}$, $T_\uparrow^{(n)} = T_\uparrow^{(1)}$, and $\alpha_\uparrow^{(n)} = \alpha_\uparrow^{(1)}$,
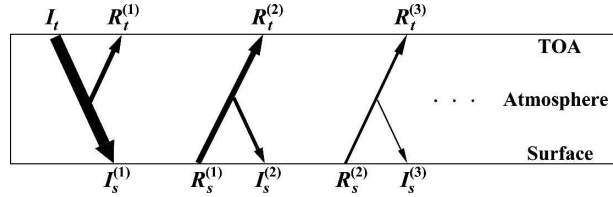

FIG. 3. Schematic drawing of an idealized radiative transfer model. Incoming solar radiation at the TOA (I_t) first travels through the atmosphere. Part of it ($R_t^{(1)} = I_t\alpha_\downarrow$) is reflected directly back to space by the atmosphere, part ($I_t A_\downarrow$) is absorbed by the atmosphere, and the rest ($I_s^{(1)} = I_t T_\downarrow$) reaches the surface. The surface absorbs part of the radiation reaching the surface [$I_t T_\downarrow (1 - \alpha_s^{(1)})$] and reflects the rest ($R_s^{(1)} = I_t T_\downarrow \alpha_s^{(1)}$) toward the atmosphere. When this surface-reflected solar radiation travels upward through the atmosphere, part of it ($I_t T_\downarrow \alpha_s^{(1)} A_\uparrow^{(1)}$) is absorbed by the atmosphere, part ($R_s^{(2)} = I_t T_\downarrow \alpha_s^{(1)} T_\uparrow^{(1)}$) reaches the TOA, and the rest ($I_s^{(2)} = I_t T_\downarrow \alpha_s^{(1)} \alpha_\uparrow^{(1)}$) is reflected back to the surface. Then, multiple reflection between the surface and atmosphere is initiated.

where the superscript n represents all integers other than 1. This assumption is not perfect, since $\alpha_s^{(n)}$, $T_\uparrow^{(n)}$, and $\alpha_\uparrow^{(n)}$ are broadband values and thus would be expected to vary as the spectrum of incoming ($I_s^{(n)}$) and upwelling ($R_s^{(n)}$) solar radiation at the surface changes with each successive reflection. However, the $\alpha_s^{(n)}$, $T_\uparrow^{(n)}$, and $\alpha_\uparrow^{(n)}$ tend each to be strongly correlated with $\alpha_s^{(1)}$, $T_\uparrow^{(1)}$, and $\alpha_\uparrow^{(1)}$. Moreover, most reflected solar radiation at the TOA is contained in the first two terms

TABLE 1. Definitions of variables, where n represents positive integers.

I_t	Incoming solar radiation at the TOA
R_t	Total upwelling solar radiation at the TOA
$R_t^{(n)}$	Different components of upwelling solar radiation at the TOA
I_s	Total downwelling solar radiation at the surface
$I_s^{(n)}$	Different components of downwelling solar radiation at the surface
R_s	Total upwelling solar radiation at the surface
$R_s^{(n)}$	Different components of upwelling solar radiation at the surface
α_p	Planetary albedo
$\alpha_s^{(n)}$	Albedo of the surface to incoming solar radiation at the surface ($I_s^{(n)}$)
$\alpha_\downarrow$	Albedo of the atmosphere to incoming solar radiation at the TOA (I_t)
$\alpha_\uparrow^{(n)}$	Albedo of the atmosphere to upwelling solar radiation from the surface ($R_s^{(n)}$)
$T_\downarrow$	Transmissivity of the atmosphere to incoming solar radiation at the TOA (I_t)
$T_\uparrow^{(n)}$	Transmissivity of the atmosphere to upwelling solar radiation from the surface ($R_s^{(n)}$)
$A_\downarrow$	Absorptivity of the atmosphere to incoming solar radiation at the TOA (I_t)
$A_\uparrow^{(n)}$	Absorptivity of the atmosphere to upwelling solar radiation from the surface ($R_s^{(n)}$)

on the right side of Eq. (1) in any case. This assumption therefore does not introduce large errors.

Using this assumption, we can modify Eq. (1):

$$R_t = I_t\alpha_\downarrow + I_tT_\downarrow\alpha_s^{(1)}T_\uparrow^{(1)} + I_tT_\downarrow\alpha_s^{(1)}\alpha_\uparrow^{(1)}\alpha_s^{(1)}T_\uparrow^{(1)} + \cdots$$

$$= I_t\alpha_\downarrow + I_t\frac{T_\downarrow T_\uparrow^{(1)}\alpha_s^{(1)}}{1 - \alpha_\uparrow^{(1)}\alpha_s^{(1)}}. \tag{2}$$

Dividing the terms on both sides of Eq. (2) by I_t, we obtain an equation governing planetary albedo (α_p):

$$\alpha_p = \alpha_\downarrow + \left(\frac{T_\downarrow T_\uparrow}{1 - \alpha_\uparrow\alpha_s}\right)\alpha_s = \alpha_\downarrow + T_e*\alpha_s, \tag{3}$$

where $T_e = T_\downarrow T_\uparrow/(1-\alpha_\uparrow\alpha_s)$. Note that for simplicity we eliminate the superscript (1) in Eq. (3).

This equation yields insight into what controls planetary albedo. According to Eq. (3), planetary albedo has two components: the albedo of the atmosphere to downwelling shortwave radiation ($\alpha_\downarrow$) and effective surface albedo ($T_e^*\alpha_s$), which can be interpreted as surface albedo (α_s) modulated by an attenuation coefficient involving shortwave radiative properties of the atmosphere (T_e). The numerator of this coefficient, $T_\downarrow T_\uparrow$, alters the surface's contribution to planetary albedo in two ways. First, the atmosphere absorbs and scatters incoming solar radiation ($T_\downarrow$), reducing the number of photons ultimately reaching the surface. Second, the atmosphere absorbs and scatters solar radiation reflected by the surface ($T_\uparrow$), preventing these photons from reaching the TOA. Since both $T_\downarrow$ and $T_\uparrow$ are smaller than unity, the surface's contribution to planetary albedo is always damped by these two effects. Moreover, since $T_\downarrow$ and $T_\uparrow$ decrease as the atmosphere becomes more opaque, the surface has a smaller contribution to planetary albedo if atmospheric optical thickness increases or if solar zenith angle becomes higher. The denominator of the attenuation coefficient, $1 - \alpha_\uparrow\alpha_s$, arises from multiple surface–atmosphere reflection. It tends to amplify the effective surface contribution by increasing the number of photons initially reflected by the surface that ultimately reach the TOA. In most regions, however, $\alpha_\uparrow\alpha_s$ is close to zero, making this amplifying effect negligible. Because the attenuation coefficient is largely dependent on $T_\downarrow$ and $T_\uparrow$, we call it effective transmissivity hereafter.

Based on Eq. (3) and our definition of T_e, effective transmissivity, we obtain an equation governing climatological seasonal-mean planetary albedo ($\bar\alpha_p$):

$$\bar\alpha_p = \bar\alpha_\downarrow + \bar{T}_e\bar\alpha_s + \overline{T'_e\alpha'_s}, \tag{4}$$

where $\bar\alpha_\downarrow$, $\bar\alpha_s$, and $\bar{T}_e$ are climatological seasonal-mean atmospheric albedo, surface albedo, and effective trans-

missivity; T'_e and α'_s are interannual seasonal-mean effective transmissivity anomalies and surface albedo anomalies. Note that the third term on the right side of Eq. (4) represents the contribution of the covariance between interannual anomalies in effective transmissivity and surface albedo to climatological seasonal-mean planetary albedo. We can also obtain an equation governing interannual seasonal-mean planetary albedo anomalies (α'_p) by subtracting Eq. (4) from Eq. (3):

$$\alpha'_p = \alpha'_\downarrow + T'_e\bar\alpha_s + \bar{T}_e\alpha'_s + T'_e\alpha'_s - \overline{T'_e\alpha'_s}, \tag{5}$$

where $\alpha'_\downarrow$ represents interannual seasonal-mean anomalies in atmospheric albedo.

5. Surface versus atmosphere

In this section, we use Eqs. (4) and (5) to quantify surface and atmospheric contributions to planetary albedo variability on seasonal and interannual time scales.

a. Separating surface and atmospheric contributions

In Eqs. (4) and (5), $\bar\alpha_s$, $\bar\alpha_p$, α'_s, and α'_p are given by the ISCCP flux datasets, and thus unknown quantities are $\bar\alpha_\downarrow$, $\bar{T}_e$, $\alpha'_\downarrow$, and T'_e. In this section, we describe a regression method to calculate them.

Because clouds are likely the main sources of fluctuations in atmospheric albedo ($\alpha'_\downarrow$) and effective transmissivity (T'_e), we express these quantities as a linear combination of cloud anomalies associated with cloud cover variations and cloud anomalies associated with cloud optical thickness variations as follows: $\alpha'_\downarrow = \gamma_1 c' + \gamma_2\varphi'$ and $T'_e = \gamma_3 c' + \gamma_4\varphi'$. Here, c' and φ' are seasonal-mean anomalies in cloud cover and the logarithm of cloud optical thickness (τ), defined as $\ln(\tau + 1)$, both calculated from the ISCCP cloud datasets; γ_1, γ_2, γ_3, and γ_4 are the linear regression coefficients relating c' and φ' to $\alpha'_\downarrow$ and T'_e. We use φ rather than τ to take account of the quasi-logarithmic dependence of cloud albedo and transmissivity on cloud optical thickness (Rossow et al. 1996). For the sake of simplicity, we call φ cloud optical thickness hereafter. Plugging these two expressions into Eq. (5) and rearranging, we obtain

$$\alpha'_p \approx \gamma_1 c' + \gamma_2\varphi' + \gamma_3(c'\alpha'_s - \overline{c'\alpha'_s} + \bar\alpha_s c')$$
$$+ \gamma_4(\varphi'\alpha'_s - \overline{\varphi'\alpha'_s} + \bar\alpha_s\varphi') + \bar{T}_e\alpha'_\downarrow. \tag{6}$$

In this equation, the terms involving the product of cloud anomalies and surface albedo anomalies, $c'\alpha'_s - \overline{c'\alpha'_s}$ and $\varphi'\alpha'_s - \overline{\varphi'\alpha'_s}$, are each expected to be negligible compared to $\bar\alpha_s c'$ and $\bar\alpha_s\varphi'$, therefore we disregard them in the subsequent analysis. To be consistent with this

assumption, we also disregard the term of $\overline{T'_e \alpha'_s}$ in Eq. (4). Under these assumptions, Eqs. (4) and (6) become

$$\overline{\alpha}_p \approx \overline{\alpha}_\downarrow + \overline{T}_e \overline{\alpha}_s \quad \text{and} \tag{7}$$

$$\alpha'_p \approx \gamma_1 c' + \gamma_2 \varphi' + \gamma_3(\overline{\alpha}_s c') + \gamma_4(\overline{\alpha}_s \varphi') + \overline{T}_e \alpha'_s. \tag{8}$$

We can regress α'_p onto c', φ', $\overline{\alpha}_s c'$, $\overline{\alpha}_s \varphi'$, and α'_s to obtain values of γ_1, γ_2, γ_3, γ_4, and $\overline{T}_e$. This is done separately for three different cryosphere regions: NH snow-covered land areas, NH sea ice zone, and Southern Hemisphere (SH) sea ice zone. These regions are defined as areas covered by snow or sea ice during seasons when snow or sea ice extent reaches a maximum (see details in caption of Fig. 4).

We perform the regression calculation based on the time series at all locations within each of these regions. This provides samples large enough to achieve stable statistics, the size of samples being greater than 10 000. The assumption here is that c', φ', $\overline{\alpha}_s c'$, $\overline{\alpha}_s \varphi'$, and α'_s generate planetary albedo anomalies in the same manner at all locations within each cryosphere region. Because the regression model accounts for more than 90% of planetary albedo variance over all cryosphere regions (see details in section 5c) and because the sample size is large, we can say with confidence that the exact values of γ_1, γ_2, γ_3, γ_4, and $\overline{T}_e$ are close to those calculated from the regression model. Once values of $\overline{T}_e$ are known, we use them to obtain values of $\overline{\alpha}_\downarrow$, based on Eq. (7). All quantities in Eqs. (7) and (8) are now known. We will use them in the subsequent sections to examine surface and atmospheric contributions to seasonal and interannual planetary albedo variability over various cryosphere regions.

b. Seasonal cycle

Figure 4 shows climatological seasonal-mean effective surface albedo (black bars), atmospheric albedo (gray bars), and planetary albedo (white bars) over NH snow-covered land areas, NH sea ice zone, and SH sea ice zone for each season, calculated from Eq. (7). A comparison of the black and gray bars reveals that effective surface albedo is much smaller than atmospheric albedo in all regions at all times of year. This demonstrates that the atmosphere is the dominant contributor to climatological planetary albedo. The dominance of the atmosphere in the climatological case can be attributed mostly to the damping effect of the atmosphere on the surface contribution, represented by effective transmissivity ($\overline{T}_e$). As shown in the gray bars in Fig. 5, values of $\overline{T}_e$ range from 0.25 to 0.4, reducing effective surface albedo to less than half of atmospheric albedo even during seasons with extensive sea ice and snow extent.
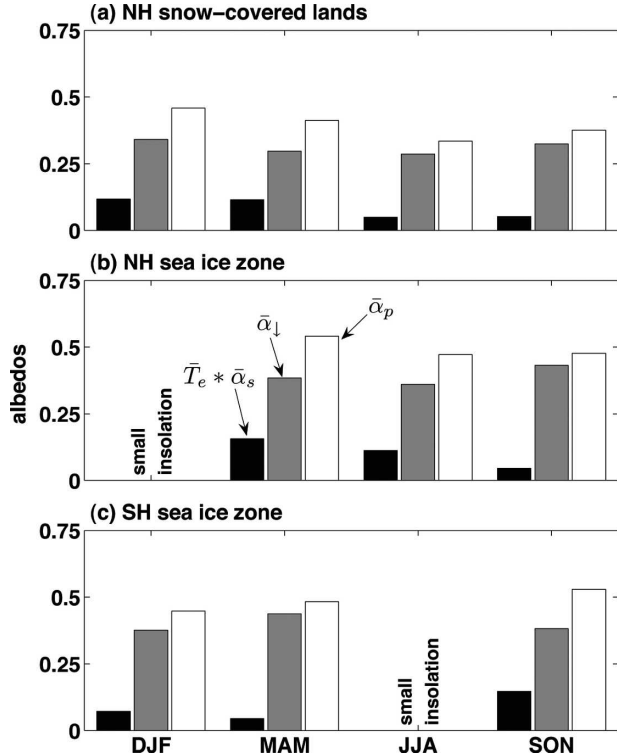

FIG. 4. Seasonal breakdown of climatological effective surface albedo ($\overline{T}_e * \overline{\alpha}_s$, black bars), atmospheric albedo ($\overline{\alpha}_\downarrow$, gray bars), and planetary albedo ($\overline{\alpha}_p$, white bars) over (a) NH snow-covered lands, (b) NH sea ice zone, and (c) SH sea ice zone. These values were calculated based on Eqs. (7) and (8) as follows: First, the seasonal-mean time series of planetary albedo, surface albedo, cloud cover, and the logarithm of cloud optical thickness were calculated based on the ISCCP D-series flux and cloud datasets. Since solar radiation varies on time scales shorter than one season, 3-h cloud cover and the logarithm of cloud optical thickness were weighted by incoming solar insolation at the TOA to give appropriate weight to cloud variations occurring when insolation is large. Based on these time series, climatological seasonal-mean planetary albedo ($\overline{\alpha}_p$), climatological seasonal-mean surface albedo ($\overline{\alpha}_s$), and the seasonal-mean anomalies in planetary albedo (α'_p), surface albedo (α'_s), cloud cover (c'), and the logarithm of cloud optical thickness (φ') were calculated. Then, α'_p was regressed onto c', φ', $\overline{\alpha}_s c'$, $\overline{\alpha}_s \varphi'$, and α'_s to obtain values of γ_1, γ_2, γ_3, γ_4, and $\overline{T}_e$ in Eq. (8) in three cryosphere regions: NH snow-covered land areas, NH sea ice zone, and SH sea ice zone. Finally, climatological seasonal-mean atmospheric albedo ($\overline{\alpha}_\downarrow$) was calculated by plugging $\overline{\alpha}_s$, $\overline{\alpha}_p$, and $\overline{T}_e$ into Eq. (7) and was averaged over the three regions, together with $\overline{\alpha}_p$ and $\overline{T}_e * \overline{\alpha}_s$. In the calculations of area averages, all three quantities were weighted by the climatological seasonal-mean incoming solar radiation at the TOA. Note that NH snow-covered lands are defined as NH lands covered by snow at least once in winter during the period of ISCCP (1984–2000), including the Greenland ice sheet; NH (SH) sea ice zone is defined as the area north (south) of 50°N (50°S) covered by sea ice at least once in spring during the period of ISCCP.
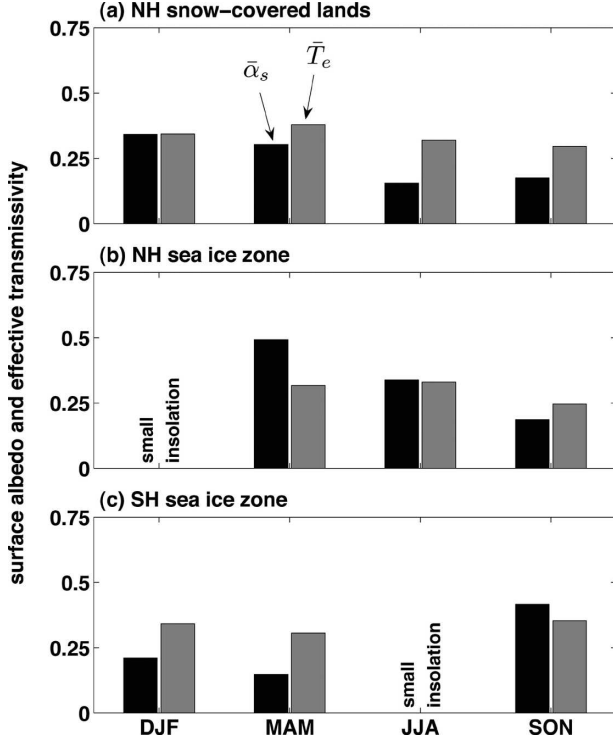
FIG. 5. Seasonal breakdown of climatological surface albedo ($\overline{\alpha}_s$, black bars) and effective transmissivity ($\overline{T}_e$, gray bars) over (a) NH snow-covered lands, (b) NH sea ice zone, and (c) SH sea ice zone.

An examination of the black bars in Fig. 4 reveals that effective surface albedo shows a small seasonal variation over all regions. Effective surface albedo in NH snow-covered land areas is about one-eighth during DJF and MAM, and shrinks by 50% during JJA and SON. This is largely consistent with seasonal variations in surface albedo (black bars in Fig. 5a, and also see Fig. 1a), rather than seasonal variations in effective transmissivity (gray bars in Fig. 5a). This in turn is due to seasonal variations of snow cover in the NH extratropics—more extensive during DJF and MAM than JJA and SON. Effective surface albedo undergoes a small seasonal variation in both sea ice zones. It is similar in both hemispheres, being largest during the springtime of each hemisphere, smallest during fall, and in between during summer. This is also largely consistent with seasonal variations in surface albedo—largest during spring, smallest during fall, and in between during summer (black bars in Figs. 5b,c, and also see Fig. 1a).

As shown in the gray bars in Fig. 4, atmospheric albedo also shows a small seasonal variation over all regions. It is smaller during spring and summer than winter and fall. For example, atmospheric albedo in NH snow-covered land areas is larger in DJF and SON than MAM and JJA. This difference is almost certainly as-

sociated with seasonal variations in the position of the earth to the sun, represented by solar zenith angle. Larger zenith angles during winter and fall in high latitudes increase the optical path of incoming solar photons, thus enhancing the albedo of the atmosphere.

Planetary albedo in NH snow-covered land areas (white bars in Fig. 4a) is largest in DJF, smallest in JJA, and in between in MAM and SON (also see Fig. 1b). This can be explained by a combination of effective surface albedo and atmospheric albedo. During winter, larger effective surface albedo coincides with higher atmospheric albedo. On the other hand, during summer, relatively small effective surface albedo coincides with lower atmosphere albedo. In the sea ice zones, planetary albedo is larger in spring than summer and fall, corresponding to the larger effective surface albedo in spring. Planetary albedo does not show appreciable differences between summer and fall (also see Fig. 1b). This is because effective surface albedo and atmospheric albedo are out of phase during these two seasons, and thus compensate each other.

As stated in section 1, the main goal of this work is to assess surface and cloud contributions to planetary albedo variability. However, much of the seasonal variation of atmospheric albedo shown in Fig. 4 is most likely caused by seasonal variations in zenith angles, rather than seasonal variations in clouds. To isolate the cloud contribution, here we focus on surface and atmospheric contributions to changes in planetary albedo within seasons with similar zenith angles, rather than to a full seasonal cycle. Based on Eq. (7), changes in planetary albedo ($\Delta\overline{\alpha}_p$) between winter and fall (spring and summer) can be written as follows:

$$
\begin{aligned}
\Delta\overline{\alpha}_p &= \overline{\alpha}_p^{\text{s1}} - \overline{\alpha}_p^{\text{s2}} \\
&= [\overline{\alpha}_{\downarrow}^{\text{s1}} + \overline{T}_e^{\text{s1}}\overline{\alpha}_s^{\text{s1}}] - [\overline{\alpha}_{\downarrow}^{\text{s2}} + \overline{T}_e^{\text{s2}}\overline{\alpha}_s^{\text{s2}}] \\
&= [\overline{\alpha}_{\downarrow}^{\text{s1}} - \overline{\alpha}_{\downarrow}^{\text{s2}}] + [(\overline{\alpha}_s^{\text{s1}} + \overline{\alpha}_s^{\text{s2}})/2](\overline{T}_e^{\text{s1}} - \overline{T}_e^{\text{s2}}) \\
&\quad + [(\overline{T}_e^{\text{s1}} + \overline{T}_e^{\text{s2}})/2](\overline{\alpha}_s^{\text{s1}} - \overline{\alpha}_s^{\text{s2}}),
\end{aligned}
\tag{9}
$$

where the superscripts s1 and s2 represent DJF and SON or MAM and JJA in NH snow-covered land areas, MAM and JJA in NH sea ice zone, and SON and DJF in SH sea ice zone. In Eq. (9), $[\overline{\alpha}_{\downarrow}^{\text{s1}} - \overline{\alpha}_{\downarrow}^{\text{s2}}] + [(\overline{\alpha}_s^{\text{s1}} + \overline{\alpha}_s^{\text{s2}})/2](\overline{T}_e^{\text{s1}} - \overline{T}_e^{\text{s2}})$ represents the change in planetary albedo due to changes in atmospheric albedo and effective transmissivity, referred to as the overall contribution of the atmosphere ($\Delta\overline{\alpha}_{pa}$); $[(\overline{T}_e^{\text{s1}} + \overline{T}_e^{\text{s2}})/2](\overline{\alpha}_s^{\text{s1}} - \overline{\alpha}_s^{\text{s2}})$ represents the change in planetary albedo due to changes in surface albedo, referred to as the contribution of the surface ($\Delta\overline{\alpha}_{ps}$). Therefore, we can simplify Eq. (9) accordingly:

$$
\Delta\overline{\alpha}_p = \Delta\overline{\alpha}_{pa} + \Delta\overline{\alpha}_{ps}.
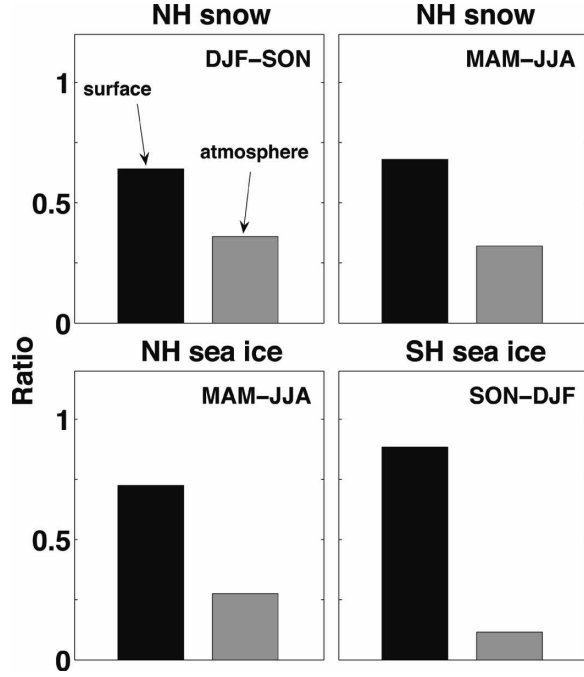\tag{10}
$$

FIG. 6. Surface (black bars) and atmospheric (gray bars) contributions to the change in planetary albedo within seasons with similar zenith angles, represented by the ratios of $\Delta\overline{\alpha}_{ps}$ and $\Delta\overline{\alpha}_{pa}$ to $\Delta\overline{\alpha}_p$ over NH snow-covered lands, NH sea ice zone, and SH sea ice zone.

Figure 6 shows values of $\Delta\overline{\alpha}_{pa}$ and $\Delta\overline{\alpha}_{ps}$ normalized by $\Delta\overline{\alpha}_p$ in NH snow-covered land areas, and NH and SH sea ice zones. In contrast to the climatological case, shown in Fig. 4, the surface contribution (black bars in Fig. 6) overwhelms the atmospheric contribution (gray bars in Fig. 6) in all three regions. The surface accounts for about 75% of the change in planetary albedo from DJF to SON and that from MAM to JJA in NH cryosphere regions. In SH sea ice zone, the surface accounts for nearly all the planetary albedo changes from SON to DJF. As shown in Table 2, this is due to the fact that the change in surface albedo ($\overline{\alpha}_s^{s1} - \overline{\alpha}_s^{s2}$) within seasons with similar zenith angles is significantly larger than planetary albedo changes due to the atmosphere ($\Delta\overline{\alpha}_{pa}$). The fact that in all cryosphere regions the surface dominates changes in planetary albedo from one season to another with similar zenith angle suggests that clouds play very little role in the seasonal cycle of planetary albedo.

c. Interannual variability

In this section, we use Eq. (8) to examine surface and cloud contributions to interannual variability in planetary albedo. Based on this equation, the variance of planetary albedo can be attributed to four terms:

$$\langle(\alpha_p')^2\rangle = \langle(\alpha_{ps}')^2\rangle + \langle(\alpha_{pc}')^2\rangle + \langle(\alpha_{pv}')^2\rangle + \langle(\alpha_r')^2\rangle, \quad (11)$$

where $(\alpha_{ps}')^2$, $(\alpha_{pc}')^2$, and $(\alpha_{pv}')^2$ are contributions of surface albedo fluctuations, cloud fluctuations, and the covariance between them, given as follows: $(\alpha_{ps}')^2 = (\overline{T}_e\alpha_s')^2$, $(\alpha_{pc}')^2 = (\gamma_1 c' + \gamma_2 \varphi' + \gamma_3\overline{\alpha}_s c' + \gamma_4\overline{\alpha}\varphi')^2$ and $(\alpha_{pv}')^2 = 2(\gamma_1 c' + \gamma_2 \varphi' + \gamma_3\overline{\alpha}_s c' + \gamma_4\overline{\alpha}\varphi')(\overline{T}_e\alpha_s')$. The residual term, $(\alpha_r')^2$, contains all variability in planetary albedo that cannot be accounted for by this regression model. Planetary albedo anomalies stemming from fluctuations in atmospheric gases, aerosols, cloud vertical structure, and cloud water phase are contained in this term. In Eq. (11), $\langle\rangle$ represents the temporal and spatial average over each cryosphere region.

The relative contributions of surface albedo fluctuations, cloud fluctuations, the covariance between them, and the residual can be quantified by dividing the terms on the right side of Eq. (11) by the variance of planetary albedo, the term on the left side of Eq. (11). Figure 7 shows the seasonal breakdown of these quantities averaged over each region. We will refer to this figure to compare the contributions of surface and clouds to interannual planetary albedo variability among regions and among seasons within the same region.

Figure 7 demonstrates that the surface (black bars) makes the dominant contribution to planetary albedo variability over all cryosphere regions at nearly all times of the year. The surface contribution is so much larger than the cloud contribution (dark gray bars in Fig. 7) mainly because $\langle(\alpha_{ps}')^2\rangle$ (gray bars in Fig. 8) is much larger than $\langle(\alpha_{pc}')^2\rangle$ (white bars in Fig. 8). This in turn is due to the large surface albedo variability asso-

TABLE 2. (first row) The change in surface albedo from winter to fall ($\overline{\alpha}_s^{s1} - \overline{\alpha}_s^{s2}$), the mean effective transmissivity over winter and fall [$(\overline{T}_e^{s1} + \overline{T}_e^{s2})/2$], and the change in planetary albedo due to the surface ($\Delta\overline{\alpha}_{ps}$) and atmosphere ($\Delta\overline{\alpha}_{pa}$) from winter to fall in NH snow-covered land areas. (second row) As in the first row except for spring and summer. (third row) As in the second row except for NH sea ice zone. (fourth row) As in the second row except for SH sea ice zone.

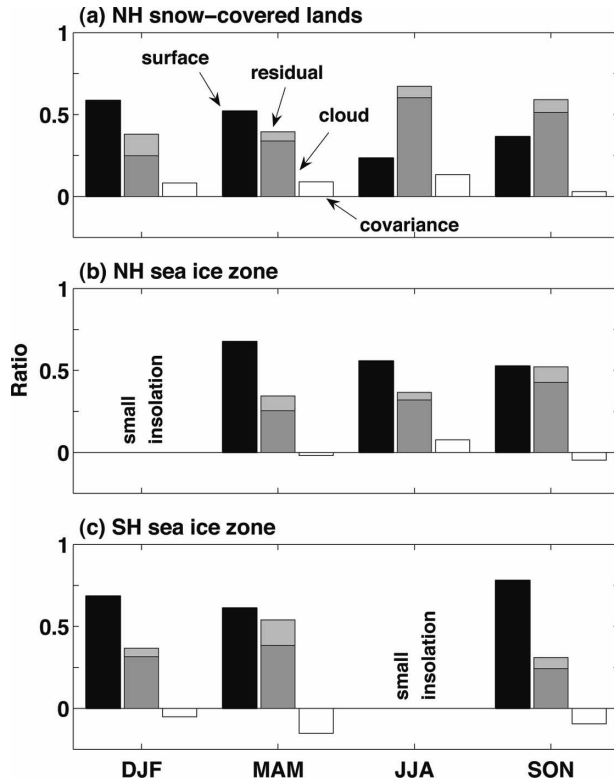| Regions	Seasons	$\overline{\alpha}_s^{s1} - \overline{\alpha}_s^{s2}$	$(\overline{T}_e^{s1} + \overline{T}_e^{s2})/2$	$\Delta\overline{\alpha}_{ps}$	$\Delta\overline{\alpha}_{pa}$
NH snow-covered lands	DJF–SON	0.166	0.319	0.053	0.030
	MAM–JJA	0.148	0.351	0.052	0.024
NH sea ice zone	MAM–JJA	0.153	0.327	0.050	0.019
SH sea ice zone	SON–DJF	0.205	0.346	0.071	0.010

FIG. 7. Ratios of surface-related planetary albedo variability $\langle(\alpha'_{ps})^2\rangle$ (black bars), cloud-related planetary albedo variability $\langle(\alpha'_{pc})^2\rangle$ (dark gray bars), residual term $\langle(\alpha'_r)^2\rangle$ (light gray bars), and covariance term $\langle(\alpha'_{pv})^2\rangle$ (white bars) to planetary albedo variability, $\langle(\alpha'_{pc})^2\rangle$, over (a) NH snow-covered lands, (b) NH sea ice zone, and (c) SH sea ice zone. These values were calculated based on Eq. (11).
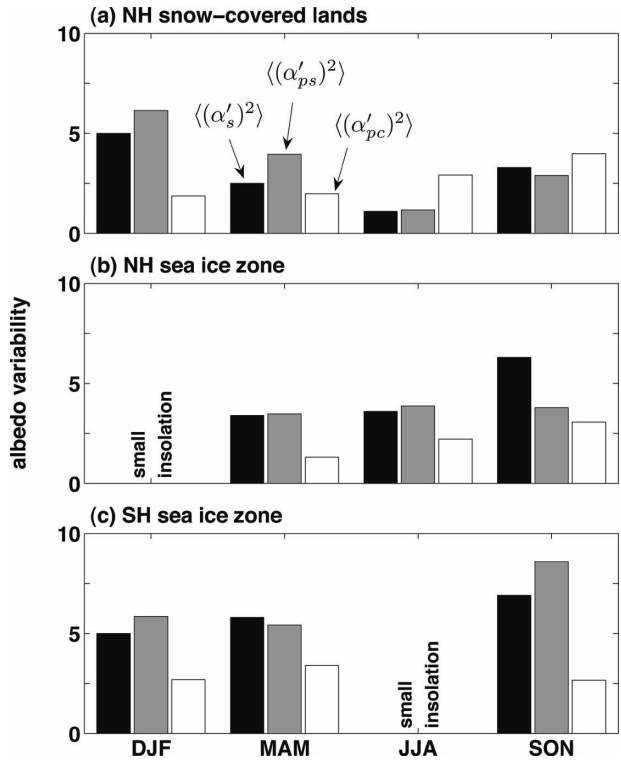

FIG. 8. Seasonal breakdown of surface albedo variability $\langle(\alpha'_s)^2\rangle$ (black bars), surface-related planetary albedo variability $\langle(\alpha'_{ps})^2\rangle$ (gray bars), and cloud-related planetary albedo variability $\langle(\alpha'_{pc})^2\rangle$ (white bars) over (a) NH snow-covered lands, (b) NH sea ice zone, and (c) SH sea ice zone. Note that the unit of $\langle(\alpha'_s)^2\rangle$ is 10^{-3}, while the unit of $\langle(\alpha'_{ps})^2\rangle$ and $\langle(\alpha'_{pc})^2\rangle$ is 10^{-4}.

ciated with snow and ice fluctuations (black bars in Fig. 8). Surface albedo variability, $\langle(\alpha'_s)^2\rangle$, associated with snow and ice fluctuations in the cryosphere regions is more than 10 times larger than planetary albedo variability due to cloud fluctuations, $\langle(\alpha'_{pc})^2\rangle$ (note that the unit of black bars in Fig. 8 is one order of magnitude larger than the unit of gray and white bars). The surface contribution is also larger in SH sea ice zone than its NH counterpart in all seasons. This is because surface albedo varies more in SH sea ice zone at all times of the year (black bars in Figs. 8b,c) and leads in turn to larger $\langle(\alpha'_{ps})^2\rangle$ (gray bars in Figs. 8b,c). This is probably also because the predominance of first-year sea ice in a divergent flow produces larger spatial variability of sea ice concentration in the SH as compared to the NH.

The surface contribution shows some seasonal variation in NH snow-covered land areas (black bars in Fig. 7a). The surface accounts for a larger fraction of the variance of planetary albedo during DJF and MAM (more than 50%) than JJA and SON (less than 50%). This is mainly due to the seasonal variation of the sur-

face albedo component of planetary albedo variability, $\langle(\alpha'_{ps})^2\rangle$ (black bars in Fig. 8). In these areas, as shown in Fig. 8, not only is the seasonal variation of $\langle(\alpha'_{ps})^2\rangle$ much larger than that of $\langle(\alpha'_{pc})^2\rangle$, but its seasonal variation is also more consistent with the surface contribution of planetary albedo variability. The seasonal variation of $\langle(\alpha'_{ps})^2\rangle$ itself—largest in winter and spring and smallest in summer and fall—can be explained by a combination of surface albedo variability and zenith angle effect. During NH winter and spring, large surface albedo variability (black bars in Fig. 8) can account for the large value of $\langle(\alpha'_{ps})^2\rangle$ compared to the two other seasons, and for the fact that this quantity is larger in winter than spring. However, differences in surface albedo variability cannot account for the larger value of $\langle(\alpha'_{ps})^2\rangle$ in spring compared to fall; surface albedo variability is actually slightly larger during SON than MAM (black bars in Fig. 8), yet $\langle(\alpha'_{ps})^2\rangle$ is 40% larger during MAM than SON. This is because in SON, large atmospheric damping effect due to high zenith angle reduces the effect of surface albedo fluctuations on planetary albedo variability. This is reflected in the larger value of

$\overline{T}_e$ in Fig. 5 during MAM (0.39) than SON (0.29). Finally, surface albedo variability subsides during JJA (black bars in Fig. 8), creating a corresponding reduction in $\langle(\alpha'_{ps})^2\rangle$.

The contribution of the covariance term (white bars in Fig. 7) is generally small (less than 10%), suggesting a very weak cloud–cryosphere interaction. As a result, a small fraction of planetary albedo variability cannot be unambiguously attributed to either cloud or surface. The fact that cloud–cryosphere interaction is weak in all cryosphere regions also suggests that clouds vary largely independently of snow and sea ice anomalies. The light gray bars in Fig. 7 reveal that the contribution of the residual is negligible (less than 10%) compared to the total contribution of surface albedo, cloud cover, and cloud optical thickness during most seasons in nearly all regions, implying that these are the factors contributing most to planetary albedo variability. This can also be viewed as a validation of our regression model and the assumptions contained within as detailed in section 5a and our implicit assumption that planetary albedo anomalies can be linearly related to anomalies in surface albedo, cloud cover, and cloud optical thickness.

6. Summary and implications

Climatological seasonal-mean planetary albedo obtained from the ISCCP D-series cloud and flux datasets in cryosphere regions was broken down into atmospheric albedo and effective surface albedo, which we define as surface albedo modulated by effective transmissivity. Atmospheric albedo accounts for much more of climatological planetary albedo ($\geq$75%) than effective surface albedo in all the regions at all times of the year. Based on the climatological seasonal-mean values of atmospheric albedo, surface albedo, and effective transmissivity, the relative contributions of the surface and atmosphere to seasonal cycle of planetary albedo in the cryosphere regions were quantified. In contrast to the climatological case, the surface is the dominant contributor to seasonal cycle of planetary albedo, accounting for about 75% of the change in planetary albedo from one season to another with similar zenith angle. The ISCCP datasets were also used to determine what controls interannual planetary albedo variability in the cryosphere regions. On an annual-mean basis, more than 90% of the variability can be linearly related to fluctuations in surface albedo, cloud cover, and the logarithm of cloud optical depth. Similar to the seasonal cycle case, the surface dominates the variability in planetary albedo, accounting for more than 50% of it at nearly all times of the year, especially during seasons with extensive snow and sea ice extent.

The different contributions of the surface in the climatological and variability cases can be understood as follows: In the climatology, the surface contribution is controlled by the relative size of surface albedo and atmospheric albedo, as well as the magnitude of the atmospheric damping effect. Surface albedo in cryosphere regions may be larger than atmospheric albedo during seasons with extensive snow and sea ice extent; however, the damping effect of the atmosphere, represented by effective transmissivity, reduces the surface contribution to less than half of the atmospheric contribution in all seasons. In the variability case, the surface contribution is controlled by the relative magnitudes of surface albedo and atmospheric albedo variability (mostly due to clouds) and the damping effect of the atmosphere. The damping effect in the variability case is exactly equal to that of the climatological case. However, surface albedo variability associated with snow and ice fluctuations in the cryosphere regions is significantly larger than atmospheric albedo variability due to cloud fluctuations. Even damped by the atmosphere to the same degree as in the climatological case, the surface contribution is therefore still dominant over the atmospheric contribution.

Although not strong enough to prevent the surface from dominating planetary albedo variability, the damping effect of the atmosphere significantly attenuates planetary albedo variability generated by surface fluctuations. For example, the magnitude of interannual planetary albedo variability in the cryosphere regions is about 10 times smaller than the magnitude of interannual surface albedo variability. This damping effect therefore partly constrains the strength of surface albedo feedback. Moreover, because this effect tends to vary seasonally, it may also contribute to seasonal variations in the strength of surface albedo feedback. For example, effective transmissivity is greater during spring than fall in NH extratropical land areas, implying that a snow albedo anomaly in NH extratropical land areas results in a larger planetary albedo anomaly in spring than fall. This is probably another reason why snow albedo feedback is stronger in spring, together with two other well-established reasons: extensive snow extent and relatively large solar radiation (e.g., Robock 1980; Hall 2004).

In this work, we demonstrate that the atmosphere is not so opaque as to prevent snow and ice anomalies from having a significant impact on TOA solar radiation. This suggests that any change in surface albedo will modify the amount of solar radiation available to the climate system. We also demonstrate that cloud–cryosphere covariability on seasonal and interannual times scales is very small in the real climate. These

results may have important implications for future climate change. Satellites have observed a retreat of NH snow cover and Arctic sea ice associated with a large-scale warming in the NH (Groisman et al. 1994; Vinnikov et al. 1999). This trend may continue in the coming decades, as a response of the climate system to anthropogenic radiative forcing such as increases in greenhouse gas concentration. Assuming cloud fields do not change much in a future climate (this is probably a valid assumption if clouds behave in the same manner in the human-induced climate change as in the seasonal and interannual internal variability contexts), our results imply that a reduction in snow and ice will lead to a significant increase in net incoming solar radiation and will thus result in more warming. This supports the idea of a positive surface albedo feedback.

Our results also highlight the fact that to faithfully simulate surface albedo feedback in climate models, it is necessary to not only reproduce the surface albedo reduction associated with a retreat of snow and sea ice, but also the damping effect of the atmosphere as this reduction is translated into a reduction in planetary albedo. Model errors in this damping effect likely stem from errors in clouds. Therefore our results point to the importance of accurately simulating the mean cloud fields in the cryosphere regions to simulate surface albedo feedback properly.

One caveat is that the credibility of our result relies on the fidelity of surface albedo variability, cloud variability, and the damping effect of the atmosphere contained in the ISCCP datasets. As Rossow and Schiffer (1999) and Hatzianastassiou et al. (2001) pointed out, the ISCCP may underestimate mean clouds in polar regions, and thus likely atmospheric damping effect. However, as shown in the appendix, this bias unlikely changes our conclusion that the surface is the dominant contributor to seasonal and interannual planetary albedo variability in cryosphere regions, assuming that the ISCCP datasets faithfully capture the magnitudes of surface albedo and cloud variability. This is probably a valid assumption because satellites used in the ISCCP measure surface reflectance and clouds by analyzing their spatial and temporal variability and are thus more likely to capture the variability in surface albedo and clouds than the mean.

APPENDIX

Sensitivity Studies

Rossow and Schiffer (1999) and Hatzianastassiou et al. (2001) pointed out that the ISCCP appears to underestimate summertime cloud cover in polar regions. In this section, we demonstrate that this bias is unlikely to change our conclusion that the surface is the dominant contributor to seasonal and interannual planetary albedo variability in cryosphere regions.

The low bias in the ISCCP summertime cloud cover may have two implications for our analysis in the previous sections: First, we probably underestimate the damping effect of the atmosphere on the surface's contribution to planetary albedo variability during summer. Second, we may underestimate atmospheric albedo ($\overline{\alpha}_\downarrow$) during that season. Below, we demonstrate that taking into account potential errors does not change our conclusion that the surface dominates planetary albedo variability. Because most of NH snow-covered land areas and SH sea ice zone are located outside polar regions, here we focus on NH sea ice zone, likely the region most vulnerable to this bias.

First of all, we correct the summertime value of effective transmissivity in NH sea ice zone through the following expression: $\tilde{\overline{T}}_e = \overline{T}_e - [(\overline{T}_e - \overline{T}_e^{cr})/\overline{c}]\Delta c$, where $\tilde{\overline{T}}_e$ is the corrected effective transmissivity; $\overline{T}_e^{cr}$ is the clear-sky effective transmissivity, which is calculated by regressing clear-sky planetary albedo anomalies onto clear-sky surface albedo anomalies in NH sea ice zone; $\overline{c}$ is the climatological summertime cloud cover (71%) given by the ISCCP; and Δc is the potential bias in the ISCCP climatological summertime cloud cover, defined as the difference in climatological summertime cloud cover between ISCCP and surface observations. According to Rossow and Schiffer (1999) and Hatzianastassiou et al. (2001), in the surface observations, values of 80% seem reasonable. Thus, we choose Δc to be 10%. The assumption behind the correction is that the attenuation effect of clouds on the surface's contribution to planetary albedo variability is proportional to climatological seasonal-mean cloud cover. We also correct the summertime value of atmospheric albedo through the expression, $\tilde{\overline{\alpha}}_\downarrow = \overline{\alpha}_\downarrow + [(\overline{\alpha}_\downarrow - \overline{\alpha}_\downarrow^{cr})/\overline{c}]\Delta c$, where $\tilde{\overline{\alpha}}_\downarrow$ is the corrected atmospheric albedo and $\overline{\alpha}_\downarrow^{cr}$ is the clear-sky atmospheric albedo, which is calculated by plugging the clear-sky values of planetary albedo, surface albedo, and effective transmissivity into Eq. (7). Here, we assume that cloud albedo is proportional to climatological seasonal-mean cloud cover.

Once $\tilde{\overline{T}}_e$ and $\tilde{\overline{\alpha}}_\downarrow$ are known, we can obtain the corrected values of $\Delta\overline{\alpha}_{pa}$, $\Delta\overline{\alpha}_{ps}$ and $\langle(\alpha'_{ps})^2\rangle$, represented by

TABLE A1. Summertime values of $\Delta\bar{\alpha}_{ps}$, $\Delta\bar{\alpha}_{pa}$, $\langle(\alpha'_{ps})^2\rangle$, $\Delta\bar{\tilde{\alpha}}_{ps}$, $\Delta\bar{\tilde{\alpha}}_{pa}$, $\langle(\tilde{\alpha}'_{ps})^2\rangle$, and $\langle(\alpha'_{pc})^2\rangle$ in the NH sea ice zone. Note that the unit of $\langle(\alpha'_{ps})^2\rangle$, $\langle(\tilde{\alpha}'_{ps})^2\rangle$, and $\langle(\alpha'_{pc})^2\rangle$ is 10^{-3}.

$\Delta\bar{\alpha}_{ps}$	$\Delta\bar{\alpha}_{pa}$	$\langle(\alpha'_{ps})^2\rangle$	$\Delta\bar{\tilde{\alpha}}_{ps}$	$\Delta\bar{\tilde{\alpha}}_{pa}$	$\langle(\tilde{\alpha}'_{ps})^2\rangle$	$\langle(\alpha'_{pc})^2\rangle$
0.050	0.019	0.387	0.047	0.022	0.304	0.222

$\Delta\bar{\tilde{\alpha}}_{pa}$, $\Delta\bar{\tilde{\alpha}}_{ps}$ and $\langle(\tilde{\alpha}'_{ps})^2\rangle$. Values of $\Delta\bar{\alpha}_{pa}$, $\Delta\bar{\alpha}_{ps}$, $\langle(\alpha'_{ps})^2\rangle$, $\Delta\bar{\tilde{\alpha}}_{pa}$, $\Delta\bar{\tilde{\alpha}}_{ps}$, and $\langle(\tilde{\alpha}'_{ps})^2\rangle$ are shown in Table A1. For comparison, the cloud contribution to interannual planetary albedo variability, $\langle(\alpha'_{pc})^2\rangle$, is also shown in the table. Here, we assume that this quantity is not affected by the bias in summertime cloud cover. (There is no evidence that ISCCP has a bias in Arctic summertime cloud variability, only that it systematically underestimates mean cloud cover.) Table A1 shows that $\Delta\bar{\tilde{\alpha}}_{ps}$ is slightly smaller than $\Delta\bar{\alpha}_{ps}$. This is due to smaller effective transmissivity, associated with more clouds during summer. For the same reason, $\langle(\tilde{\alpha}'_{ps})^2\rangle$ is also smaller than $\langle(\alpha'_{ps})^2\rangle$. Even when cloud cover is increased by 10%, the surface contributions [$\Delta\bar{\tilde{\alpha}}_{ps}$ and $\langle(\tilde{\alpha}'_{ps})^2\rangle$] to seasonal and interannual planetary albedo variability are still larger than the atmospheric contributions [$\Delta\bar{\tilde{\alpha}}_{pa}$ and $\langle(\alpha'_{pc})^2\rangle$]. This implies that the bias in the ISCCP climatological summertime mean cloud cover does not change our result that the surface is the dominant contributor to planetary albedo variability on seasonal and interannual time scales in NH sea ice zone.

The potential bias in the ISCCP climatological mean clouds probably also occurs in NH sea ice zone during other seasons or in other cryosphere regions. However, since NH summertime sea ice zone may be the most vulnerable case, we believe that this bias will unlikely change our conclusion that the surface dominates planetary albedo variability in cryosphere regions.

REFERENCES

Budyko, M. I., 1969: The effect of solar radiation variations on the climate of the earth. *Tellus,* **21,** 611–619.

Gloersen, P., C. L. Parkinson, D. J. Cavalieri, J. C. Comiso, and H. J. Zwally, 1999: Spatial distribution of trends and seasonality in the hemispheric sea ice covers: 1978–1996. *J. Geophys. Res.,* **104** (C9), 20 827–20 835.

Groisman, P. Y., T. R. Karl, and R. W. Knight, 1994: Observed impact of snow cover on the heat balance and the rise of continental spring temperatures. *Science,* **263,** 198–200.

Grotjahn, R., 1993: Zonal average observations. *Global Atmospheric Circulations: Observations and Theories,* Oxford University Press, 39–89.

Hall, A., 2004: The role of surface albedo feedback in climate. *J. Climate,* **17,** 1550–1568.

Hatzianastassiou, N., N. Cleridou, and I. Vardavas, 2001: Polar

cloud climatologies from ISCCP C2 and D2. *J. Climate,* **14,** 3851–3862.

Kiehl, J. T., and K. E. Trenberth, 1997: Earth's annual global mean energy budget. *Bull. Amer. Meteor. Soc.,* **78,** 197–208.

Kukla, G., and D. Robinson, 1980: Annual cycle of surface albedo. *Mon. Wea. Rev.,* **108,** 56–68.

Laine, V., and M. Heikinheimo, 1996: Estimation of surface albedo from NOAA AVHRR data in high latitudes. *Tellus,* **48A,** 424–441.

Liou, K. N., 1992: Introduction. *Radiation and Cloud Processes in the Atmosphere,* Oxford University Press, 3–19.

Manabe, S., and R. J. Stouffer, 1980: Sensitivity of a global climate model to an increase of CO_2 concentration in the atmosphere. *J. Geophys. Res.,* **85** (C10), 5529–5554.

Parkinson, C. L., 1991: Interannual variability of the spatial distribution of sea ice in the north polar region. *J. Geophys. Res.,* **96** (C3), 4791–4801.

——, 1992: Interannual variability of monthly southern ocean sea ice distributions. *J. Geophys. Res.,* **97** (C4), 5349–5363.

Robinson, D. A., K. F. Dewey, and R. R. Heim Jr., 1993: Global snow cover monitoring: An update. *Bull. Amer. Meteor. Soc.,* **74,** 1689–1696.

Robock, A., 1980: The seasonal cycle of snow cover, sea ice and surface albedo. *Mon. Wea. Rev.,* **108,** 267–285.

——, 1983: Ice and snow feedbacks and the latitudinal and seasonal distribution of climate sensitivity. *J. Atmos. Sci.,* **40,** 986–997.

Rossow, W. B., and R. A. Schiffer, 1991: ISCCP cloud data products. *Bull. Amer. Meteor. Soc.,* **72,** 2–20.

——, and L. C. Garder, 1993a: Cloud detection using satellite measurements of infrared and visible radiances for ISCCP. *J. Climate,* **6,** 2341–2369.

——, and ——, 1993b: Validation of ISCCP cloud detections. *J. Climate,* **6,** 2370–2393.

——, and R. A. Schiffer, 1999: Advances in understanding clouds from ISCCP. *Bull. Amer. Meteor. Soc.,* **80,** 2261–2287.

——, A. W. Walker, and L. C. Garder, 1993: Comparison of ISCCP and other cloud amounts. *J. Climate,* **6,** 2394–2418.

——, ——, D. Beuschel, and M. Roiter, 1996: International Satellite Cloud Climatological Project (ISCCP) description of new cloud datasets. WMO/TD 737, World Climate Research Programme (ICSU AND WMO), 115 pp.

Sellers, W. D., 1969: A global climatic model based on the energy balance of the earth-atmosphere system. *J. Appl. Meteor.,* **8,** 392–400.

Vinnikov, K. Y., and Coauthors, 1999: Global warming and Northern Hemisphere sea ice extent. *Science,* **286,** 1934–1937.

——, A. Robock, D. J. Cavalieri, and C. L. Parkinson, 2002: Analysis of seasonal cycles in climatic trends with application to satellite observations of sea ice extent. *Geophys. Res. Lett.,* **29,** 1310, doi:10.1029/2001GL014481.

Walland, D. J., and I. Simmonds, 1997: North American and Eurasian snow cover covariability. *Tellus,* **49A,** 503–512.

Zhang, Y.-C., W. B. Rossow, A. A. Lacis, V. Oinas, and M. M. Mishchenko, 2004: Calculation of radiative fluxes from the surface to top of atmosphere based on ISCCP and other global datasets: Refinements of the radiative transfer model and the input data. *J. Geophys. Res.,* **109,** D19105, doi:10.1029/2003JD004457.